Experimental Studies of the Two-Plasmon-Decay Instability in Long-Scale-Length Plasmas

Introduction

Direct-drive inertial confinement fusion (ICF) is an encouraging path to high-gain inertial fusion energy.[1] In the direct-drive approach to ICF, high-power, moderate-intensity laser beams ($\sim 7 \times 10^{14}$ W/cm^2) produce and propagate through a high-temperature ($T_e \sim 3.5$ keV), long-scale-length ($L_n \sim 500$ μm) underdense plasma prior to depositing energy near the critical surface of a spherical capsule. A series of shocks are launched that adiabatically compress the nuclear fuel to fusion conditions.[2–4] For the most-efficient compression, the shocks are driven on a low adiabat[5] and ignition is susceptible to preheat; heating of the imploding shell by "hot" electrons increases the implosion adiabat, reducing the compression efficiency.

Electrons can be accelerated to high energies by two-plasmon-decay (TPD) instability[6] in which the incident electromagnetic wave decays into two electron-plasma waves.[7–9] The instability grows rapidly through the resonant coupling of the electric field of the incident laser beam and the longitudinal electrostatic field of the two electron-plasma waves. The dependence of TPD on the hydrodynamic conditions is evident in the convective (intensity) gain exponent for the instability of a single-plane electromagnetic wave [$G_{SB} \simeq 1.9 \times 10^{-2}\, I_s\, (\times 10^{14}\ \mathrm{W/cm^2})\, L_n\, (\mu\mathrm{m}) \big/ T_e(\mathrm{keV})$, where I_s is the single-beam intensity, L_n is the density scale length, T_e is the electron temperature, and all parameters are taken at $n_{cr}/4$, $n_{cr} \simeq 10^{22}$ cm^{-3}] (Ref. 10). Simulations based on a nonlinear Zakharov model[11] that includes test particles, indicate that electrons are stochastically accelerated to high energies (>50 keV) by enhanced electron-plasma waves. Once above threshold, the hot-electron temperature is shown to scale with $I_q L_n / T_e$ (Ref. 12), where I_q is the overlapped intensity at quarter critical.

Early experiments using CO_2 lasers measured the first hot electrons generated by TPD[13] and the associated electron-plasma waves using Thomson scattering.[14] More-recent experiments focusing on TPD in direct-drive–ignition conditions[15] demonstrated that the efficiency of hot-electron generation scaled with overlapped laser-beam intensity.[16] These studies showed a nearly constant electron temperature and saturation of the hot-electron generation at 0.1% of the incident laser energy when plotted as a function of the vacuum laser intensity.[17] This apparent saturation and low level of electron generation were results of the hydrodynamics; the small laser spots used to produce the highest intensities limited the scale length to less than $L_n < 200$ μm.

The work presented in this article uses the large laser spots and high ultraviolet intensities available on OMEGA EP[18] to produce a 400-μm-long-scale-length, 2.5-keV plasma, where $I_q L_n / T_e$ is increased by nearly a factor of 4 when the laser intensity is varied from 1.3 to 7×10^{14} W/cm^2. Over this range in intensities, a rapid increase in the hot-electron temperature (25 keV to 90 keV) is measured and for intensities above 3.5×10^{14} W/cm^2 the hot-electron efficiency generation is saturated at a nearly constant level of ~1% of the incident laser energy.[19] The rapid increase in hot-electron temperature is compared with simulations that use a Zakharov model designed to provide a physics-based predictive capability for TPD at ignition conditions.[20]

Experimental Setup

1. Target and Laser Configuration

The experimental configuration is shown in Fig. 129.23, where the long-scale-length CH plasma was produced by illuminating a 30-μm-thick CH layer deposited on 30 μm of Mo and backed with an additional 30 μm of CH. The CH thickness was chosen to avoid any burnthrough to the Mo layer. This was verified by the fact that no Mo spectral lines were observed except for the inner-shell K lines that were attributed to the TPD hot electrons. The Mo thickness was equal to a range of electrons with a typical energy of ~120 keV, which was confirmed by Monte Carlo simulations that showed that electrons with energies less than 120 keV were stopped within the Mo. This resulted in nearly all of the electrons accelerated by TPD being absorbed in the target.

The 17.5-keV Mo K_α line was sufficiently high in energy to ensure that photoexcitation from the $T_e \simeq 2.5$-keV coronal plasma region did not contribute to the K_α-emission measure-

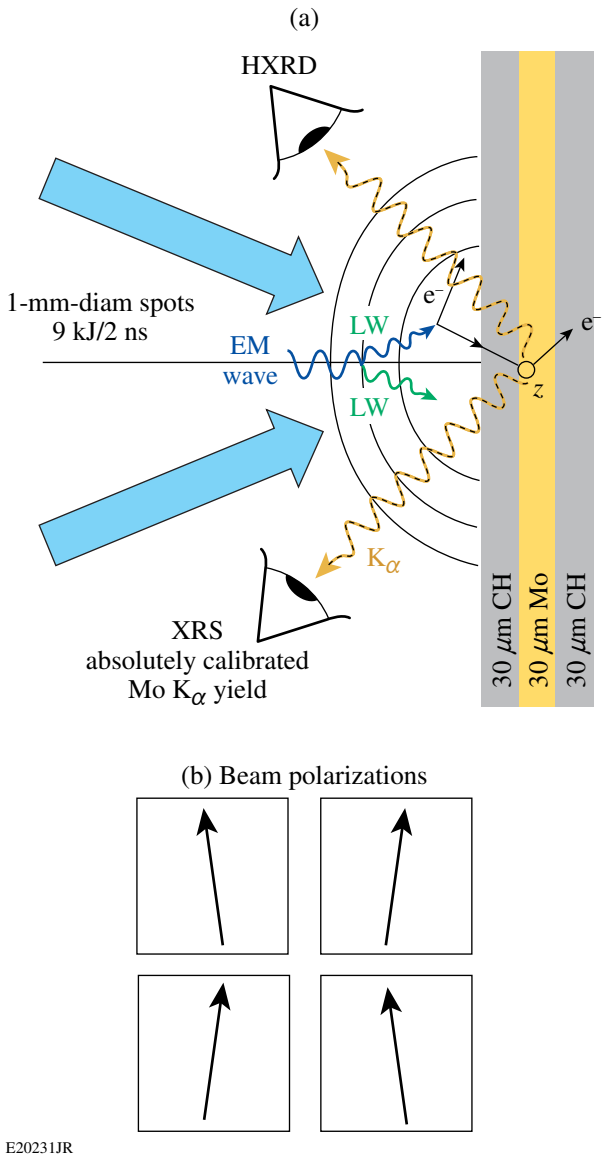

Figure 129.23
(a) The 2-mm × 2-mm target is illuminated by four UV laser beams. The 30-μm-thick Mo is used to capture the majority of the electrons produced by TPD. (b) The polarization of each laser beam is 8° from vertical as shown.

ments. This ensured that the measured K_α emission was a result of K-shell impact and hard x-ray photoionization caused by the hot electrons produced by TPD. This is confirmed by integrating the measured x-ray continuum above the K_α energy [$E(K_\alpha)$ = 17.5 keV] to obtain the total number of x rays (N). Assuming that all x rays are absorbed in the Mo, an upper bound for the contribution of the continuum to the K_α yield is $E_R \cong E(K_\alpha)\,\omega_k N$, where ω_k is the fluorescence yield. Even for the highest laser irradiance, the contribution of the x-ray continuum to the K_α yield is only a few percent of the measured K_α energy; therefore, the radiation contribution is negligible. There is an additional effect of K_α excitation by the bremsstrahlung emitted by the hot electrons; this secondary effect is included in the Monte Carlo–code calculations described in **Diagnostics** (p. 23), which were used to derive the total energy in hot electrons.

For this study, four ultraviolet ($\lambda_0 = 0.35\ \mu$m) beams available from the OMEGA EP Laser System[18] produced the required intensities over a large-diameter laser spot to create 400-μm plasma density scale lengths at $n_{cr}/4$ (Fig. 129.24). A maximum overlapped laser intensity of 7×10^{14} W/cm^2 was achieved using a total energy on target of 8.7 kJ in a 2-ns flattop laser pulse (Fig. 129.24). The four UV beams intersect the target at an angle of 23° with respect to the target normal and are linearly polarized

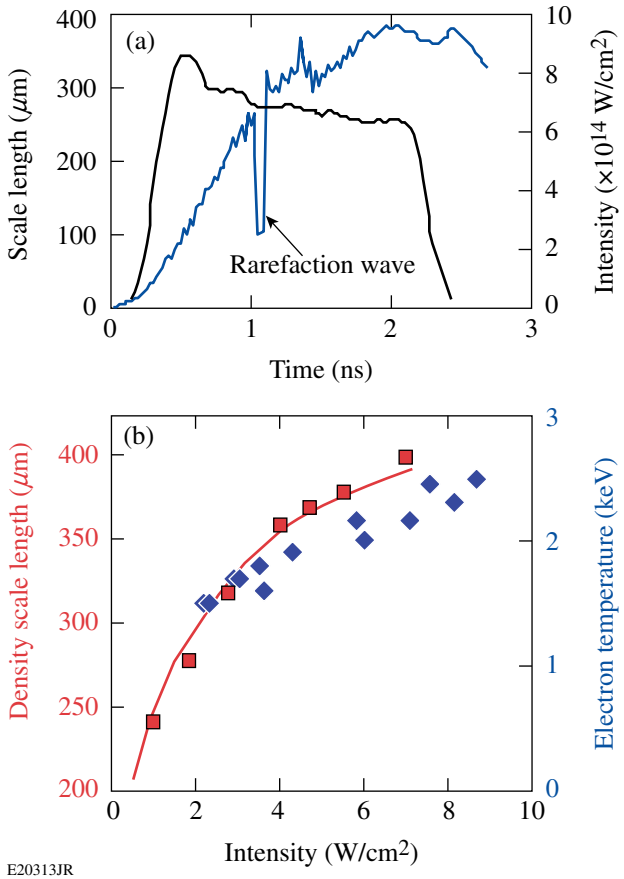

Figure 129.24
(a) The high UV laser power available (P_{max} = 4.5 TW) on OMEGA EP provides the necessary intensity (right axis) over a nearly 1-mm-diam laser spot to produce an electron-density scale length $L_n \simeq 400\ \mu$m. The simulated plasma scale length (left axis) increases to saturation after ~1.5 ns. (b) The maximum simulated density scale length (left axis) and electron temperature (right axis) at quarter critical are shown as a function of the overlapped intensity.

[Fig. 129.23(b)]. Two sets of distributed phase plates (DPP's)[21] were used (840-μm and 890-μm diameter measured at the 1/e intensity points) to produce a combined intensity distribution that has a super-Gaussian profile with a diameter of nearly 1 mm.

Figure 129.25 shows a time-integrated x-ray pinhole image of the focal spot. This radiation is emitted by the laser-heated CH layer and characterizes the interaction region. The x-ray profile in Fig. 129.25(b) has a width (at half-maximum) that is similar to that of the overlapped vacuum laser profile, but the flattop of the latter has been rounded in the x-ray image; this is mainly a result of the lateral heat conduction within the plasma.

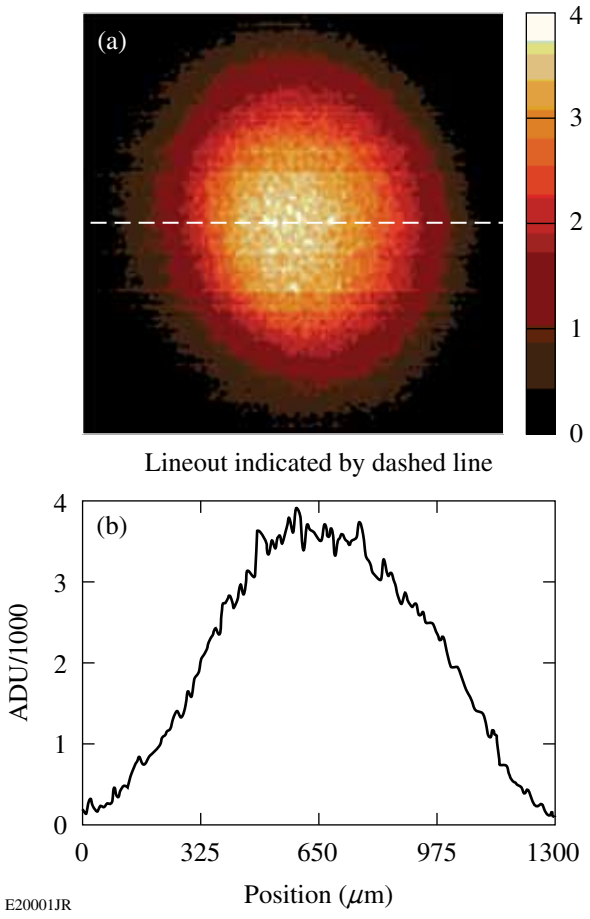

Figure 129.25
(a) X-ray image of the irradiated focal spot at 5×10^{14} W/cm^2 (in the photon-energy range of 2 to 7 keV). (b) This lineout is indicated by the horizontal dashed line in the image in (a).

2. Hydrodynamics

a. Simulations. Two-dimensional hydrodynamic simulations using the codes *SAGE*[22] and *DRACO*[23] show that the maximum-achievable scale length in planar geometry is obtained by maximizing the overlapped-laser-beam intensity while providing enough time for the plasma to reach steady state. Figure 129.24(a) shows that increasing the overlapped-laser-beam intensity increases both the scale length and the electron temperature at quarter critical $\left(L_n/T_e \approx 160\ \mu\text{m/keV}\right)$. Over this intensity range, the hydrodynamic simulations indicate that the intensity of the laser beams at $n_{cr}/4$, where TPD has the largest growth rate, is reduced from the vacuum intensity by ~55%. For the highest laser-beam energies available at 2 ns, the optimal laser spot size is ~1-mm diameter; a further increase in laser-spot size reduces the intensity on target, resulting in a shorter scale length. For the experimental conditions presented here, the scale length reaches a steady state after about 1.5 ns [Fig. 129.24(b)] and the asymptotic scale length is given by $L_n \simeq 250\ \mu\text{m}\ \langle I_{14} \rangle^{1/4}$.

b. X-ray continuum measurements. To check the reliability of the simulations, comparisons were made between calculated and measured plasma conditions at quarter critical and time- and space-integrated x-ray fluence in the energy range of ~5 to 8 keV. This radiation is emitted in the laser-heated CH layer. An example (using *SAGE*) from a shot at an irradiance of 2.7×10^{14} W/cm^2 is shown in Fig. 129.26. No intensity normalization was applied. Even though most of the radiation comes from layers deeper (and colder) than the quarter-critical surface, the ability of the codes to replicate the x-ray fluence in absolute magnitude makes the calculated plasma parameters (such as the TPD threshold below) credible.

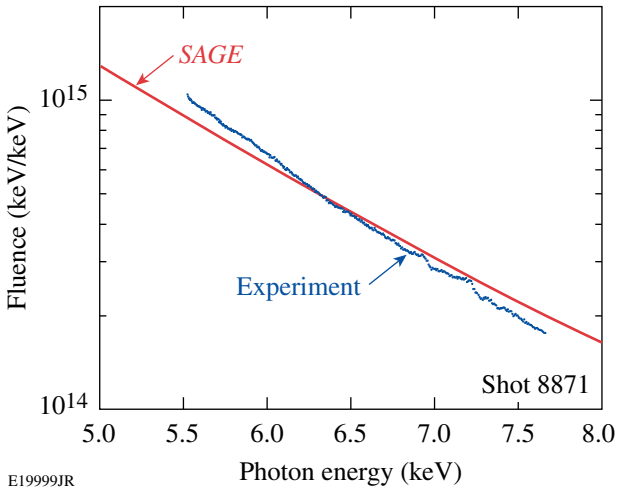

Figure 129.26
SAGE-calculated x-ray fluence from a shot at an irradiance of 2.7×10^{14} W/cm^2. No normalization of intensity was applied.

c. UV Thomson-scattering measurements. A more-rigorous test of the calculated plasma parameters was obtained using

Thomson scattering.[19] Figure 129.27 shows a Thomson-scattering spectrum where the ion-acoustic features are resolved and used to measure the electron and ion temperatures. The measured electron temperature is within a few percent of the simulations [Fig. 129.27(c)].

The rarefaction wave launched from the CH/Mo interface is observed in the Thomson-scattering spectrum 1.11 ns after the laser beams turns on, which is in excellent agreement with the hydrodynamic simulations [Fig. 129.24(a)]. Although the density scale length at quarter critical is not directly measured, the excellent agreement between the measured and simulated time of arrival of the rarefaction wave demonstrates the accuracy of the thermal conduction model and is a strong indication that the calculated density and temperature profiles are accurate.

The Thomson-scattering measurements were obtained on the OMEGA Laser System using the same target platform, pulse shape, and similar laser beam diameters (800-μm FWHM) as used on the OMEGA EP experiments. A 20-J, $\lambda_{4\omega} = 0.26$-μm, *f*/6.7 Thomson-scattering probe beam was focused to a diameter of 60 μm and the Thomson-scattered light was collected from a 60-μm × 75-μm × 75-μm volume located 200 μm from the initial target surface.[24] The Thomson-scattering diagnostic probes ion-acoustic waves propagating nearly parallel to the target [$k_a = 2\, k_{4\omega} \sin(\theta/2)$, where $k_{4\omega} = 2\pi/\lambda_{4\omega}$ and $\theta = 63°$ is the scattering angle].

3. Diagnostics

a. X-ray spectrometer. The determination of total hot-electron energy depends on an absolute calibration of the spectrometers measuring the Mo K_α line (at 17.5 keV). An x-ray spectrometer was used for all shots but checked for consistency on several shots by comparison with a Cauchois-type quartz crystal spectrometer (TCS)[26] and single-hit charge-coupled–device (CCD) array (SPC).[27] The energy in the Mo K_α-emission line (E_{K_α}) was measured using an absolutely calibrated planar LiF crystal spectrometer (XRS) that views the target from the incident laser side at an angle of 63° from the target normal [Fig. 129.23(a)].[28]

The LiF crystal was calibrated by LLE and the quartz crystal at NIST.[29] The CCD array (Spectral Instruments[30] model 800) was calibrated by Maddox *et al.*[31] for several photon energies, including correction for background. XRS and TCS used image plates to record the spectra; calibration data for the same plates and image scanner as used at LLE were published by Meadowcroft *et al.*[32] The results of the three instruments for a single shot at 6.4×10^{14} W/cm^2 are shown in Fig. 129.28. The energy in the Mo K_α line from the XRS and TCS spectra agrees to within 15%; that from TCS agrees with the first two to within 25%. The slightly different spectral resolution of the instruments does not impact the measurement of the total K_α energy. The agreement with the CCD instrument is particularly significant since, unlike the other two spectrometers, it does not use image plates. Figure 129.29 shows that the energy con-

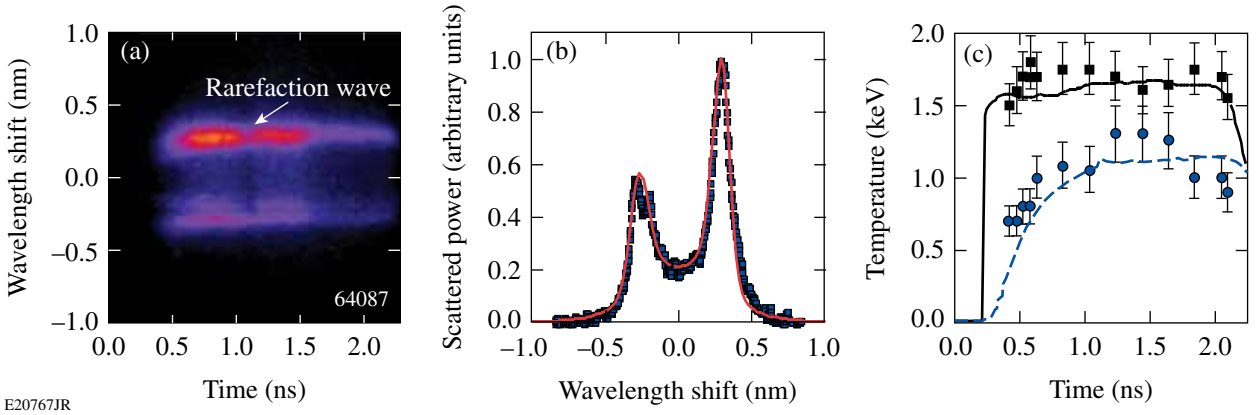

Figure 129.27

(a) Thomson-scattered light from near the quarter critical density for 3ω light is spectrally and temporally resolved to measure the ion-acoustic features. The electron and ion temperatures as a function of time are obtained by fitting the standard dynamic form factor[25] to the measured spectra that are averaged over 50 ps. (b) A best fit (red curve) to the measured spectrum at 0.8 ns (blue) is obtained for $T_e = 1.6$ keV, $T_i = 1.0$ keV. (c) The electron (solid) and ion (dashed) temperatures calculated by *DRACO* compare well to the measurements.

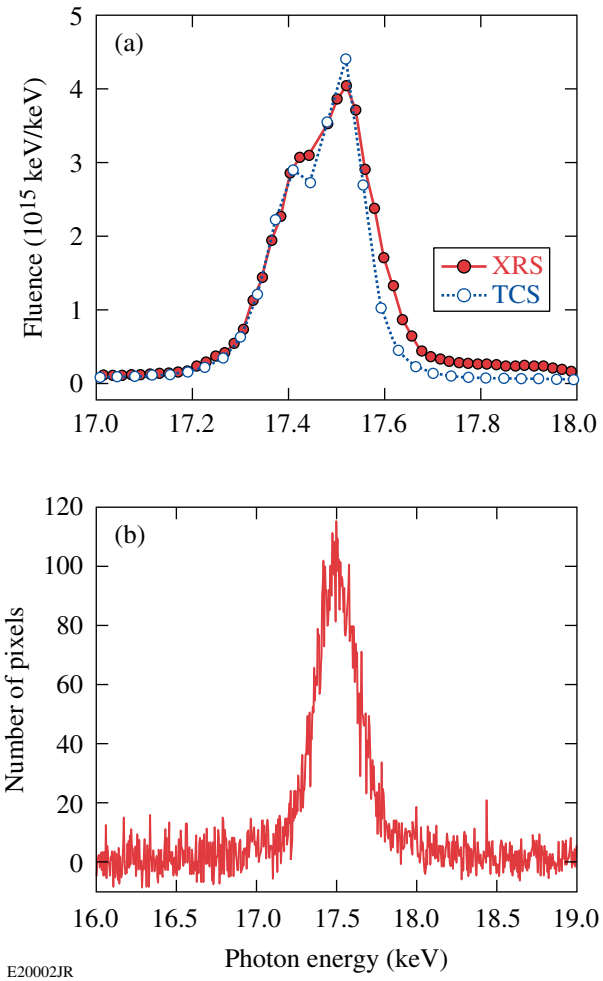

Figure 129.28
An example of the Mo K_α spectra measured on a single shot by three detectors: (a) a planar LiF crystal spectrometer and a Cauchois-type quartz crystal spectrometer and (b) a single-hit CCD array (SPC). The three measurements of K_α energy are consistent.

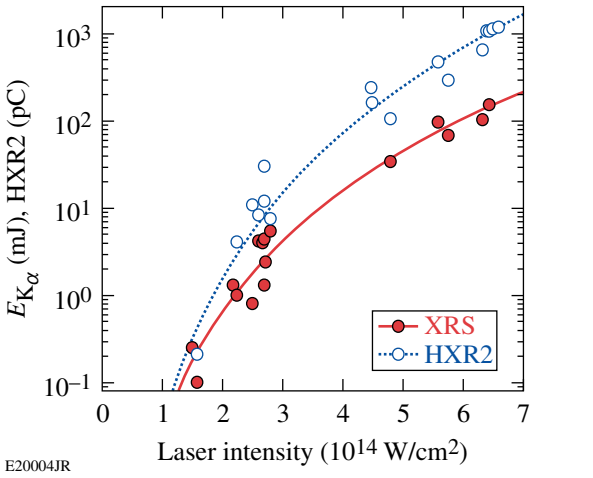

Figure 129.29
Mo K_α and hard x-ray (≳40-keV) yields. Both signals rise rapidly with laser intensity.

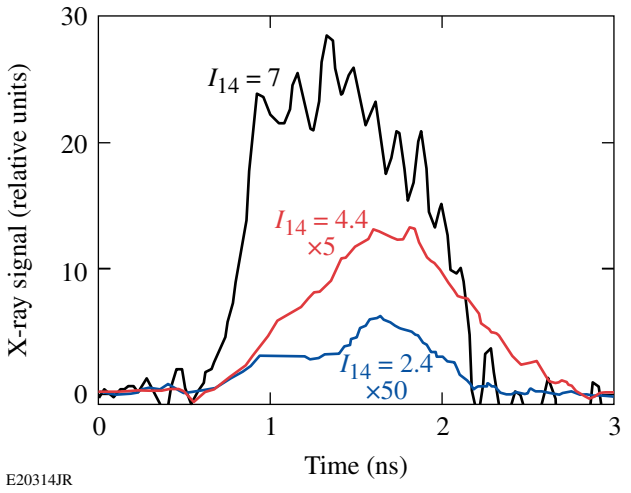

Figure 129.30
The measured hard x-ray emission (>40 keV) is shown for overlapped intensities of 7×10^{14} W/cm^2 (black), 4.4×10^{14} W/cm^2 (red), and 2.4×10^{14} W/cm^2 (blue).

tained within the Mo K_α line scales quasi-exponentially with laser intensity over nearly four orders of magnitude when the vacuum laser intensity is varied from 1.3 to 7×10^{14} W/cm^2.

b. Hard x-ray detector (HXRD). Figure 129.30 shows the hard x-ray emission as a function of time for one of the three x-ray channels used to measure the hot-electron temperature. The hot-electron temperature (T_{hot}) is assumed to be equal to the slope of the hard x-ray radiation that is determined by fitting an exponential decay [$\exp(-E/T_{hot})$] to the measured ratios of the x-ray radiation above ~40 keV, ~60 keV, and ~80 keV obtained using a three-channel scintillator detector (HXRD).[33]

The hard x-ray scaling provides an additional signature of hot-electron generation. Figure 129.29 compares the scaling with laser intensity of the K_α and bremsstrahlung yields. Both signals increase quasi-exponentially by several orders of magnitude, primarily because of the increase in the number of hot electrons. The hard x rays rise faster as a result of the corresponding increase in hot-electron temperature with intensity shown in **Results** (p. 26). This occurs because the bremsstrahlung emission increases with hot-electron temperature, whereas the cross section for Mo K_α excitation decreases with electron energy above ~50 keV.

c. Monte Carlo simulations. Monte Carlo simulations using the code *EGSnrc*[34] are used to relate the measured Mo K_α energy and the HXRD signal to the total energy in hot electrons. For the electron spectra discussed in this article (T_{hot} = 25 to 90 keV), the Monte Carlo simulations indicate that the total electron energy is directly related to the total K_α energy given the hot-electron temperature $E_{electrons}(J) \simeq 150\, E_{K_\alpha}(mJ/sr)/\sqrt{T_{hot}(keV)}$. This relationship is accurate to within 20% over the relevant hot-electron temperature range and is specific to the geometry of the experiment.

The Monte Carlo code calculates both the K_α and the associated bremsstrahlung spectrum (HXR) given an initial electron-beam spectrum. Both the K_α and HXR yields are calculated as functions of the observation angle. To obtain reliable results, 10^7 electrons are typically assumed to be normally incident on the target with a Maxwellian energy distribution at the experimentally determined temperature T_{hot}. The number of calculated K_α photons and HXR photons per energy bin is typically of the order of 10^3; therefore, a statistical precision of a few percent is obtained.

The calculated K_α energy was tested by comparison with experiment. Reference 35 shows extensive measurements of the Cu K_α line from an x-ray tube as a function of emission angle and tube voltage. The corresponding Monte Carlo simulations (assuming a monoenergetic electron beam) agree very closely with Ref. 35. The temperature of the input-electron distribution is taken to be the measured slope of the HXR. Figure 129.31 shows that the two temperatures are essentially the same; for an assumed electron temperature of 80 keV, the HXR slope is 79 keV.

Changing the assumed hot-electron divergence has a small effect on the calculated K_α signal because (a) the range of most electrons is smaller than the Mo thickness, (b) electron scattering changes the initially monodirectional distribution into a quasi-isotropic distribution, and (c) the target is large compared to the focal-spot size. This simplifies the determination of hot-electron generation but also precludes studying the electron divergence, which is important for determining preheat in spherical implosions. A similar situation exists with respect to the HXR radiation. For a low-Z target and unidirectional electrons, the HXR spectrum is peaked in the forward direction. The Monte Carlo–code calculations show that because of electron scattering in the Mo; however, the spectrum becomes quasi-isotropic in intensity and in shape (therefore T_{hot} is uniquely defined). Again, the spectrum is independent of initial electron divergence.

Before comparing the measured and simulated K_α energies, it is necessary to account for the angular dependence of K_α emission. The local emission of K_α is strictly isotropic, but its opacity through the molybdenum creates an angular distribution. Figure 129.32 shows the K_α emission per unit solid angle $\Delta\Omega$ for two hot-electron temperatures. As expected, the distri-

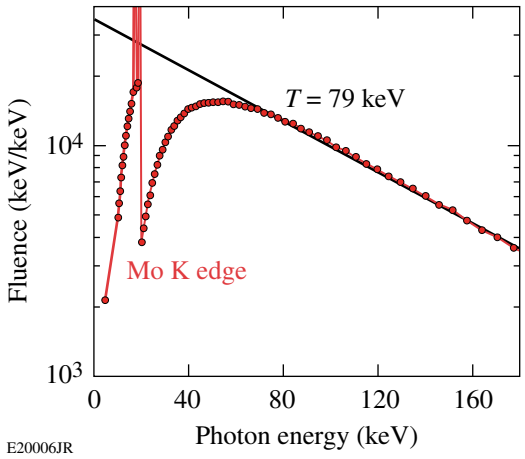

Figure 129.31
Monte Carlo–calculated HXR spectra for 10 million incident electrons. The slope of the HXR continuum (79 keV) is about equal to the hot-electron temperature assumed for the Monte Carlo–code run (80 keV). The smoothness of the curve is an indication of the good statistics obtained with 10 million electrons.

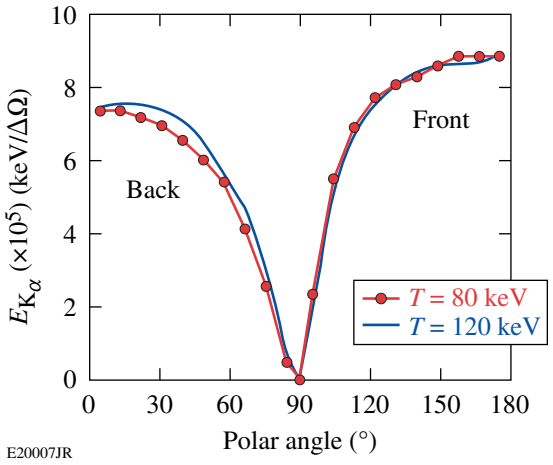

Figure 129.32
Monte Carlo–calculated angular distribution of Mo K_α as function of polar angle θ (relative to the target normal) per unit solid angle. "Back" stands for the back of the target (forward emission).

bution peaks in the forward and backward directions $\theta = 0°$ and $\theta = 180°$, where the K_α opacity is minimal. Figure 129.32 is used to relate the measured K_α emission per unit solid angle to the calculated emission in the direction of the spectrometer. The shape of the angular distribution across the detector is nearly the same for different hot-electron temperatures for the target thickness used in this study.

Based on the K_α yield calculated by the Monte Carlo code, Fig. 129.33 gives the total energy in hot electrons divided by the K_α energy per unit solid angle in the forward direction. Using Fig. 129.33, the measured energy in K_α (Fig. 129.29) can be converted into energy in hot electrons.

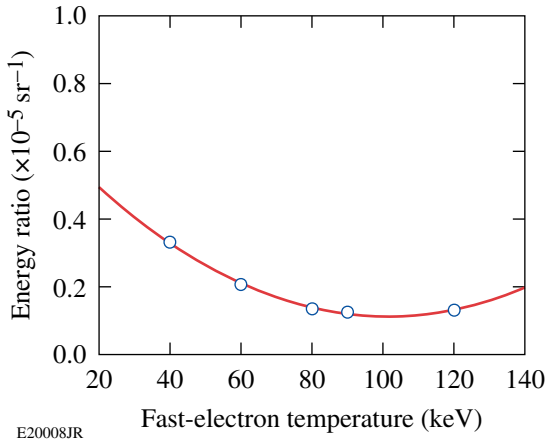

Figure 129.33
Monte Carlo–calculated ratio of the total incident electron energy and the K_α emission per unit solid angle in the target normal direction as a function of the hot-electron temperature. This curve is used to deduce the total energy in hot electrons from the measured Mo K_α energy.

Results

1. Hot-Electron Temperature

Figure 129.34(a) shows that the hot-electron temperature increases from 25 keV to 90 keV as the laser intensity is increased from 2 to 7×10^{14} W/cm^2. These experimental results are compared with calculations from two theoretical models of two-plasmon-decay instability for the exact parameters of the experiment. The open squares are results obtained from the code *ZAK*,[12] which solves the equations of the extended Zakharov model.[36] The saturating nonlinearities included in the model are density-profile modification,[37] Langmuir wave cavitation,[38] and the generation of ion-acoustic turbulence.[12,39] While this plasma fluid model is able to describe the growth and nonlinear saturation of the instability, it does not include kinetic effects responsible for hot-electron generation. An estimate for the hot-electron temperature is obtained from the nonlinearly

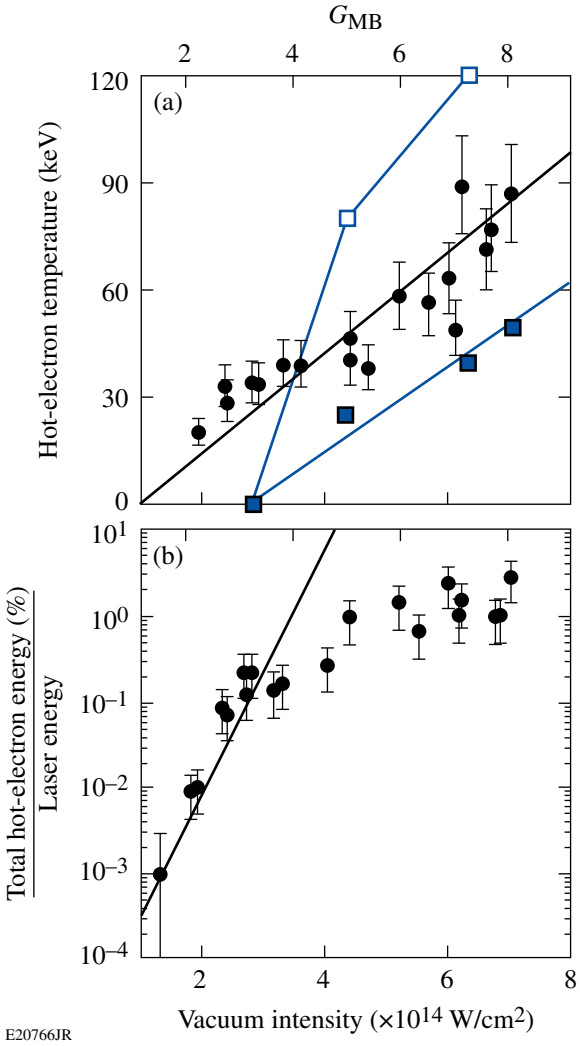

Figure 129.34
(a) The hot-electron temperature inferred from the HXRD measurements (circles) is shown as a function of the vacuum overlapped intensity and the multibeam convective gain. The hot-electron temperature is calculated by *ZAK* (open squares) and *QZAK* (solid squares) using the simulated $n_{cr}/4$ hydrodynamic parameters. (b) The fraction of total laser energy deposited into the hot electrons is plotted as a function of the vacuum overlapped intensity and the multibeam convective gain. An exponential scaling $\sim\exp\left(G_{MB}/0.3\right)$ is shown for comparison (line).

saturated state via the integration of test-electron trajectories in the electrostatic fields associated with the Langmuir turbulence (see Ref. 12 for more details).

The electron-plasma wave spectrum at saturation is found to be very broad, extending from small wave numbers up to the Landau cutoff ($k\lambda_D = 0.25$). When the effect of the turbulent electron-plasma wave spectrum on hot-electron production is investigated by integrating electron test particle trajectories,[12] the heating is found to be diffusive for electrons above a thresh-

old energy corresponding to the smallest phase velocity plasma waves (those at the Landau cutoff, $1/2 m_e v_\phi^2 \sim 20$ to 30 keV). The rate of diffusion (heating) was found to scale with $I_q L_n / T_e$ as a result of the interplay between the root-mean-square plasma-wave amplitudes and the available acceleration length.[12]

The solid squares show the results of a generalization of the *ZAK* model, called *QZAK*,[40] currently under development, where kinetic effects are taken into account self-consistently in the quasilinear approximation. The addition of kinetic effects reduces the amplitude of the electron-plasma waves, reducing the hot-electron temperature for a given $I_q L_n / T_e$. The difference between the two model predictions highlights the difficulty in making predictive calculations of a highly turbulent and complex physical system.

2. Fraction of Hot Electrons

Figure 129.34(b) shows the fraction of laser energy converted into hot electrons, which is estimated using the measured total K_α energy [Fig. 129.30(b)]. The large fraction of energy deposited into the hot electrons and the observed saturation of the TPD instability are direct consequences of the simultaneous high intensity and long scale lengths produced in these experiments.

It appears TPD is only convectively unstable in these experiments. The absolutely unstable electron-plasma waves, which depend only on the single-beam intensity, are well below the absolute intensity threshold (I_{th}) for the highest laser intensities tested;

$$\left\{\eta \equiv \frac{I_s}{I_{th}} = \frac{I_s\left(\times 10^{14}\ \mathrm{W/cm^2}\right) L_n(\mu\mathrm{m})}{230\ T_e(\mathrm{keV})} < 1\right\}$$

(Ref. 41), where I_s is the single-beam intensity at $n_{cr}/4$.

A convective gain for TPD that depends on the overlapped laser-beam intensity is presented in Ref. 42, where multiple laser beams are shown to drive common electron-plasma waves. For the experiments discussed here, the maximum convective gain is

$$G_{MB} \cong 1.5 \times 10^{-2} I_q \left(\times 10^{14}\ \mathrm{W/cm^2}\right) L_n(\mu\mathrm{m}) / T_e(\mathrm{keV}),$$

where I_q is the overlapped laser beam intensity at $n_{cr}/4$.

The multiple-beam gain is significantly larger than the single-beam gain $\left(G_{MB}/G_{SM} \simeq 3\right)$; note that the single-beam gain depends on the single-beam intensity $\left(I_s = I_q/4\right)$ and the intensity at $n_{cr}/4$ is ~55% less than the vacuum intensity. Figure 129.34 shows the experimental results plotted against the multiple-beam gain. A threshold for hot-electron generation is observed at a multiple-beam gain of ~2. It is likely that the actual gain for laser beams with DPP's (i.e., beams with speckles) is 2 to 5 times larger.[43]

At the highest overlapped-laser-beam intensity (7×10^{14} W/cm^2), the TPD gain increases approximately linearly in time over ~1.3 ns to a constant level of $G_{MB} \simeq 8$. When the gain reaches $G_{MB} \simeq 2.3$ ($t = 0.6$ ns), the hard x-ray signal begins to rapidly rise before reaching a nearly constant level [Fig. 129.30]. For the lowest intensities (1.3×10^{14} W/cm^2) where K_α radiation was detected (limited by signal to noise in the detector), the common-wave TPD gain is calculated to be $G_{MB} \simeq 2$, which is consistent with the gain threshold shown in Fig. 129.34.

Summary

This target platform was designed to account for all of the hot electrons generated by TPD. In general, the coupling of hot electrons to a fusion target will be reduced by the electron divergence, the distance between where the electrons are created and where they are absorbed, the electron energy distribution, and other loss mechanisms. The planar nature of these experiments, the fact that the laser beams are at near-normal incidence to the target, and the fact that they are linearly polarized in a common direction without polarization smoothing all tend to maximize the hot-electron generation. The multibeam linear gain depends on the geometry of the beams and their polarizations, which must be taken into account when applying these results to ignition designs.[42]

In summary, the high laser intensities generated over 1-mm-diam laser spots produced plasmas with a density scale length of 400 μm, causing two-plasmon decay to be driven to saturation. The hot-electron temperature is measured to increase rapidly (25 keV to 90 keV) with increasing laser-beam intensity (2×10^{14} W/cm^2 to 7×10^{14} W/cm^2). The total energy in hot electrons generated by TPD is measured to increase exponentially and saturate at a level of ~1% of the laser energy as the intensity is increased above 3×10^{14} W/cm^2. Uncertainties in the coupling of TPD electrons to the imploding shell and an accounting of the geometry and polarization of the laser beams prevent a quantitative assessment of the effect of TPD on direct-drive fusion, but these experiments suggest that maintaining the multibeam convective gain below 5 is a conservative approach to an acceptable level of hot-electron generation in direct-drive–ignition target designs.

ACKNOWLEDGMENT

We acknowledge the OMEGA EP operations team whose efforts provided the increased laser power necessary for these results. This work was supported by the U.S. Department of Energy Office of Inertial Confinement Fusion under Cooperative Agreement No. DE-FC52-08NA28302, the University of Rochester, and the New York State Energy Research and Development Authority. The support of DOE does not constitute an endorsement by DOE of the views expressed in this article.

REFERENCES

1. J. Nuckolls *et al.*, Nature **239**, 139 (1972).
2. R. L. McCrory, D. D. Meyerhofer, R. Betti, R. S. Craxton, J. A. Delettrez, D. H. Edgell, V. Yu Glebov, V. N. Goncharov, D. R. Harding, D. W. Jacobs-Perkins, J. P. Knauer, F. J. Marshall, P. W. McKenty, P. B. Radha, S. P. Regan, T. C. Sangster, W. Seka, R. W. Short, S. Skupsky, V. A. Smalyuk, J. M. Soures, C. Stoeckl, B. Yaakobi, D. Shvarts, J. A. Frenje, C. K. Li, R. D. Petrasso, and F. H. Séguin, Phys. Plasmas **15**, 055503 (2008).
3. T. R. Boehly, V. N. Goncharov, W. Seka, M. A. Barrios, P. M. Celliers, D. G. Hicks, G. W. Collins, S. X. Hu, J. A. Marozas, and D. D. Meyerhofer, Phys. Rev. Lett. **106**, 195005 (2011).
4. J. D. Lindl *et al.*, Phys. Plasmas **11**, 339 (2004).
5. V. N. Goncharov, T. C. Sangster, T. R. Boehly, S. X. Hu, I. V. Igumenshchev, F. J. Marshall, R. L. McCrory, D. D. Meyerhofer, P. B. Radha, W. Seka, S. Skupsky, C. Stoeckl, D. T. Casey, J. A. Frenje, and R. D. Petrasso, Phys. Rev. Lett. **104**, 165001 (2010).
6. H. Figueroa *et al.*, Phys. Fluids **27**, 1887 (1984).
7. M. V. Goldman, Ann. Phys. **38**, 95 (1966).
8. C. S. Liu, M. N. Rosenbluth, and R. B. White, Phys. Rev. Lett. **31**, 697 (1973).
9. B. B. Afeyan and E. A. Williams, Phys. Plasmas **4**, 3827 (1997).
10. M. N. Rosenbluth, R. B. White, and C. S. Liu, Phys. Rev. Lett. **31**, 1190 (1973).
11. D. F. DuBois, D. A. Russell, and H. A. Rose, Phys. Rev. Lett. **74**, 3983 (1995).
12. J. F. Myatt, J. Zhang, J. A. Delettrez, A. V. Maximov, R. W. Short, W. Seka, D. H. Edgell, D. F. DuBois, D. A. Russell, and H. X. Vu, Phys. Plasmas **19**, 022707 (2012).
13. N. A. Ebrahim *et al.*, Phys. Rev. Lett. **45**, 1179 (1980).
14. H. A. Baldis and C. J. Walsh, Phys. Rev. Lett. **47**, 1658 (1981).
15. W. Seka, D. H. Edgell, J. F. Myatt, A. V. Maximov, R. W. Short, V. N. Goncharov, and H. A. Baldis, Phys. Plasmas **16**, 052701 (2009).
16. C. Stoeckl, R. E. Bahr, B. Yaakobi, W. Seka, S. P. Regan, R. S. Craxton, J. A. Delettrez, R. W. Short, J. Myatt, A. V. Maximov, and H. Baldis, Phys. Rev. Lett. **90**, 235002 (2003).
17. An analytical error in the analysis of the HXRD used in Ref. 16 was identified and when corrected, the hot-electron temperature is reduced by ~40%.
18. J. H. Kelly, L. J. Waxer, V. Bagnoud, I. A. Begishev, J. Bromage, B. E. Kruschwitz, T. J. Kessler, S. J. Loucks, D. N. Maywar, R. L. McCrory, D. D. Meyerhofer, S. F. B. Morse, J. B. Oliver, A. L. Rigatti, A. W. Schmid, C. Stoeckl, S. Dalton, L. Folnsbee, M. J. Guardalben, R. Jungquist, J. Puth, M. J. Shoup III, D. Weiner, and J. D. Zuegel, J. Phys. IV France **133**, 75 (2006).
19. D. H. Froula, B. Yaakobi, S. X. Hu, P.-Y. Chang, R. S. Craxton, D. H. Edgell, R. Follett, D. T. Michel, J. F. Myatt, W. Seka, R. W. Short, A. Solodov, and "Saturation of the Two-Plasmon-Decay Instability in Long-Scale-Length Plasma Relevant to Direct-Drive Inertial Confinement Fusion," to be published in Physical Review Letters.
20. *LLE Review Quarterly Report* **127**, 109, Laboratory for Laser Energetics, University of Rochester, Rochester, NY, LLE Document No. DOE/NA/28302-1022 (2010).
21. T. J. Kessler, Y. Lin, J. J. Armstrong, and B. Velazquez, in *Laser Coherence Control: Technology and Applications*, edited by H. T. Powell and T. J. Kessler (SPIE, Bellingham, WA, 1993), Vol. 1870, pp. 95–104.
22. R. S. Craxton and R. L. McCrory, J. Appl. Phys. **56**, 108 (1984).
23. P. B. Radha, V. N. Goncharov, T. J. B. Collins, J. A. Delettrez, Y. Elbaz, V. Yu. Glebov, R. L. Keck, D. E. Keller, J. P. Knauer, J. A. Marozas, F. J. Marshall, P. W. McKenty, D. D. Meyerhofer, S. P. Regan, T. C. Sangster, D. Shvarts, S. Skupsky, Y. Srebro, R. P. J. Town, and C. Stoeckl, Phys. Plasmas **12**, 032702 (2005).
24. D. H. Froula, J. S. Ross, L. Divol. and S. H. Glenzer, Rev. Sci. Instrum. **77**, 10E522 (2006).
25. D. H. Froula, S. H. Glenzer, N. C. Luhmann, and J. Scheffield, *Plasma Scattering of Electromagnetic Radiation: Theory and Measurement Techniques*, 2nd ed. (Elsevier, Burlington, MA, 2011).
26. J. F. Seely *et al.*, Rev. Sci. Instrum. **81**, 10E301 (2010).
27. C. Stoeckl, W. Theobald, T. C. Sangster, M. H. Key, P. Patel, B. B. Zhang, R. Clarke, S. Karsch, and P. Norreys, Rev. Sci. Instrum. **75**, 3705 (2004).
28. B. Yaakobi, P.-Y. Chang, A. A. Solodov, C. Stoeckl, D. H. Edgell, R. S. Craxton, S. X. Hu, J. F. Myatt, F. J. Marshall, W. Seka, and D. H. Froula, Phys. Plasmas **19**, 012704 (2011).
29. U. Feldman *et al.*, Naval Research Laboratory and L. T. Hudson and S. Seltzer, National Institute of Standards and Technology, private communication (2011).
30. Spectral Instruments, Tucson, AZ 85745 (http://www.specinst.com/Products/800s_datasheet.pdf).
31. B. R. Maddox *et al.*, Rev. Sci. Instrum. **79**, 10E924 (2008).
32. A. L. Meadowcroft, C. D. Bentley, and E. N. Stott, Rev. Sci. Instrum. **79**, 113102 (2008).

33. C. Stoeckl, V. Yu. Glebov, D. D. Meyerhofer, W. Seka, B. Yaakobi, R. P. J. Town, and J. D. Zuegel, Rev. Sci. Instrum. **72**, 1197 (2001).

34. I. Kawrakow *et al*., NRC, Ottawa, Canada, NRCC Report PIRS-701 (May 2011); I. Kawrakow, Med. Phys. **27**, 485 (2000).

35. V. Metchnik and S. G. Tomlin, Proc. Phys. Soc. **81**, 956 (1963).

36. D. A. Russell and D. F. DuBois, Phys. Rev. Lett. **86**, 428 (1995).

37. A. B. Langdon, B. F. Lasinski, and W. L. Kruer, Phys. Rev. Lett. **43**, 133 (1979).

38. G. D. Doolen, D. F. DuBois, and H. A. Rose, Phys. Rev. Lett. **54**, 804 (1985).

39. R. Yan, A. V. Maximov, C. Ren, and F. S. Tsung, Phys. Rev. Lett. **103**, 175002 (2009).

40. D. A. Russell, presented at the Workshop on Laser Plasma Instabilities, sponsored by Lawrence Livermore National Laboratory and the University of Rochester's Laboratory for Laser Energetics, Livermore, CA, 3–5 April 2002.

41. A. Simon, R. W. Short, E. A. Williams, and T. Dewandre, Phys. Fluids **26**, 3107 (1983).

42. D. T. Michel, A. Maximov, B. Yaakobi, S. Hu, J. Myatt, A. Solodov, R. W. Short, and D. H. Froula, "Experimental Demonstration of the Two-Plasmon-Decay Common-Wave Process," submitted to Physical Review Letters.

43. H. A. Rose and D. F. DuBois, Phys. Rev. Lett. **72**, 2883 (1994).